Electrochemical Impedance Spectroscopy Integrated with Environmental Transmission Electron Microscopy

Ma, Zhongtao; Dacayan, Waynah Lou; Chatzichristodoulou, Christodoulos; Mølhave, Kristian Speranza; Chiabrera, Francesco Maria; Zhang, Wenjing; Simonsen, Søren Bredmose

Published in:
Small Methods

Link to article, DOI:
10.1002/smtd.202201713

Publication date:
2023

Document Version
Publisher's PDF, also known as Version of record

small methods
www.small-methods.com

Electrochemical Impedance Spectroscopy Integrated with Environmental Transmission Electron Microscopy

*Zhongtao Ma, Waynah Lou Dacayan, Christodoulos Chatzichristodoulou, Kristian Speranza Mølhave, Francesco Maria Chiabrera, Wenjing Zhang, and Søren Bredmose Simonsen**

The concept of combining electrical impedance spectroscopy (EIS) with environmental transmission electron microscopy (ETEM) is demonstrated by testing a specially designed micro gadolinia-doped ceria (CGO) sample in reactive gasses (O_2 and H_2/H_2O), at elevated temperatures (room temperature—800 °C) and with applied electrical potentials. The EIS-TEM method provides structural and compositional information with direct correlation to the electrochemical performance. It is demonstrated that reliable EIS measurements can be achieved in the TEM for a sample with nanoscale dimensions. Specifically, the ionic and electronic conductivity, the surface exchange resistivity, and the volume-specific chemical capacitance are in good agreement with results from more standardized electrochemical tests on macroscopic samples. CGO is chosen as a test material due to its relevance for solid oxide electrochemical reactions where its electrochemical performance depends on temperature and gas environment. As expected, the results show increased conductivity and lower surface exchange resistance in H_2/H_2O gas mixtures where the oxygen partial pressure is low compared to experiments in pure O_2. The developed EIS-TEM platform is an important tool in promoting the understanding of nanoscale processes for green energy technologies, e.g., solid oxide electrolysis/fuel cells, batteries, thermoelectric devices, etc.

1. Introduction

The efficiency of green energy technologies such as P2X (including electrolysis), fuel cells, and batteries directly depends on reaction rates in the involved electrochemical reactions. These again depend on the structure and composition of the component materials.[1] Comparison of electrochemical tests with post-mortem microscopy investigations shows that structural and compositional evolution at the nanoscale is the main reasons for efficiency losses.[2] To accelerate the implementation of particularly P2X and fuel cell technologies in the green energy infrastructure, a detailed understanding of the correlation between electrochemistry and structure/composition is needed so that efficient degradation mitigation strategies can be developed.

Post-mortem microscopy has led to important developments in all areas of energy technologies. However, results from post-mortem characterization only represent the end result from the entire electrochemical process history, including the effects of various gas environments, polarizations, temperature ramps, as well as possible effects from sample preparation for microscopy. In order to directly link a given electrochemical stimuli (e.g., reactant composition, temperature, electrical polarization) with the structure/composition change of the material in its active state, we need to develop a new operando characterization method that provides real-time electrochemical measurements with atomic level structure characterization under relevant conditions.

One group of methods with a potential to give insight into nanostructure/composition of materials in their active state is in situ/operando TEM. These methods allow for structure and composition investigations at high spatial resolution while exposing the sample to various selected stimuli, e.g., controlled atmospheres,[3] elevated temperature,[4] applied stress,[5] electrical polarization[6] or combinations of these.

On the other hand, an electrochemical method that can give information about the electrochemical response of the functional materials under operating conditions is electrochemical impedance spectroscopy (EIS). This has been widely used due

Z. Ma, W. L. Dacayan, C. Chatzichristodoulou, F. M. Chiabrera, S. B. Simonsen
DTU Energy
Fysikvej, 2800 Kgs. Lyngby, Denmark
E-mail: sobrs@dtu.dk
K. S. Mølhave
DTU Nanolab
Ørsteds Plads, 2800 Kgs. Lyngby, Denmark
W. Zhang
DTU Environment
Bygningstorvet, 2800 Kgs. Lyngby, Denmark

The ORCID identification number(s) for the author(s) of this article can be found under https://doi.org/10.1002/smtd.202201713

DOI: 10.1002/smtd.202201713

to its nondestructive nature, high sensitivity, and ability to study and distinguish between surface/interface and bulk processes.[7]

Electrochemical TEM investigations are already carried out at room temperature in a vacuum or in liquid phase, particularly with focus on battery materials.[8] Recently, attempts have been made to expand the electrochemical TEM capabilities to include operando experiments with focus on the solid oxide fuel and electrolysis cells (SOFC and SOEC)[9] requiring at least three stimuli: electrical potentials, reactive gases, and elevated temperatures. Today, chip-based heating-biasing TEM holders are commercially available (e.g., Protochips Fusion, DENS solutions Lightning, Hummingbird Scientific MEMS Heating Biasing, Thermo Fisher Scientific NanoEX). The combination of such holders and an environmental TEM (ETEM) offers the possibility to study the three stimuli combined.

Preparing and conducting high-temperature solid state electrochemical TEM with relevance to SOEC or SOFC is far from trivial. Here, a few of the challenges are listed: First, solid oxide electrochemical cells have complex layered structures composed of a mixture of metals and hard, brittle ceramics. These need to be thinned to electron transparency and mounted on the heating-biasing chips while ensuring mechanical stability and sufficient electrical contact to the biasing electrodes of the chip. Second, fracture of the sample or loss of electrical contract must be avoided, taking into consideration the thermal expansion of the sample and the chip components during heating. Most importantly, the currents in the chip heater must not interfere with the electrochemical measurements and should be well separated from the sample. The combination of relatively high resistivity, ρ, for the ceramic materials under investigation and the extraordinarily small dimensions of a typical TEM sample leads to very high measured resistances often in the GΩ range. It is therefore crucial to minimize the unavoidable leak currents through the chip components.

Before high-temperature solid state electrochemical TEM can exploit its full potential, it is crucial to establish that these challenges can be solved in a manner that reliable electrochemical measurements can be performed in the TEM. This we do in the present work. We present a combined EIS-TEM analysis of $Ce_{0.9}Gd_{0.1}O_{1.95-\delta}$ (CGO), which is a popular SOEC and SOFC electrolyte–electrode barrier layer material and is commonly used as a multi-functional component in the composite electrodes of the cell.[10] CGO is a good material for testing the reliability of EIS measurements because its various electrochemical properties (ionic conductivity, electronic conductivity, activity for surface-gas exchange reactions), which are dependent on temperature and the gas environment, can be measured with EIS and are well documented.

The results from this work show that the combined EIS and TEM (EIS-TEM) measurements agree with reference experiments with larger CGO samples. The EIS-TEM method also allows for establishing a direct link between the electrochemical activity and the nanoscaled structure and composition of the material. The method is not limited to investigations of SOECs/SOFCs, but can also be useful for linking functionality and structure/composition in studies of batteries, thermoelectric devices, catalysis, corrosion, etc.

This paper presents EIS-TEM measurements on a CGO sample with nanoscale dimensions. The temperature and pO_2 dependence of the ionic and electronic conductivity, as well as its surface exchange resistivity in O_2 and H_2/H_2O atmospheres, and its volume-specific chemical capacitance in H_2/H_2O, are measured. The influence of Pt porosity is studied and finally the result is shown to be reproducible.

2. Results and Discussion

2.1. Structure of the CGO Sample

Figure 1a shows an overview of the chip geometry while Figure 1b presents how the CGO sample was mounted on top of the chip. It can be observed from the latter that the sample consists of two thick side parts and a thinner central part with a thickness of ≈100 nm (according to EELS log-ratio analysis[11]). The thick side parts (Figure 1b) are connected to the chip electrodes and the thin central part spans over the hole in the center of the chip shown in Figure 1a.

The corresponding SEM-EDS map in Figure 1c shows that most of the top surface area of the side parts is covered with ion-deposited Pt. On the other hand, there is no trace of Pt on top of the thinned central CGO part, as well as on a small portion of the top surfaces of the two thick side parts and on their side surfaces. Pt is also not expected on their entire bottom surface of the sample (not visible, but with access to gas phase due to the 10° tilt between the CGO sample and the chip).

The TEM image of the thinned central part in Figure 1e shows its dimensions and reveals a single-grain boundary between two micrometer-sized grains. The presence of a single-grain boundary is consistent with the grain size of few micrometers observed in the CGO pellet (Figure 1d). Measurements on the HRTEM image (Figure 1f) of the region marked by a red square in Figure 1e are consistent with the crystal structure of $Ce_{0.9}Gd_{0.1}O_{1.95-\delta}$ with the space group $Fm3m$ observed at zone axis $[0\bar{1}1]$.[12]

2.2. Morphology and Oxidation State

Figure 2 presents an image series of the grain boundary region at temperatures from 200 °C to 800 °C, in H_2/H_2O gas environment. As could be expected from previous studies,[13] no morphological changes were observed as a response to the elevated temperature (or as a response to electron beam exposure or EIS measurements). Specifically, the sample stayed fully dense (i.e., no pores developed), the interface between the sample and air (and between the two grains) stayed straight and smooth, and no new structures were formed such as nanoparticle generating on the surface. The changes in contrast in the images can be attributed to the displacement of the sample position along the direction of the electron beam caused by thermal expansion. The sample is also stable in the O_2 environment.

It is expected that the Ce oxidation state in the CGO will be Ce^{4+} in the oxygen environment, while the amount of Ce^{3+} increases in the reducing environments, especially at the CGO surface where reduction initiates. This was confirmed by EELS Ce M_5-to-M_4 white line ratio analysis, where spectra measured in O_2 and in H_2/H_2O with ratio 0.8 showed Ce^{4+} in the central part of the thin CGO, and an increased amount of Ce^{3+} ≈10 nm near the CGO surface This is consistent with EELS analysis of pure ceria (see Section S5, Supporting Information).[14]

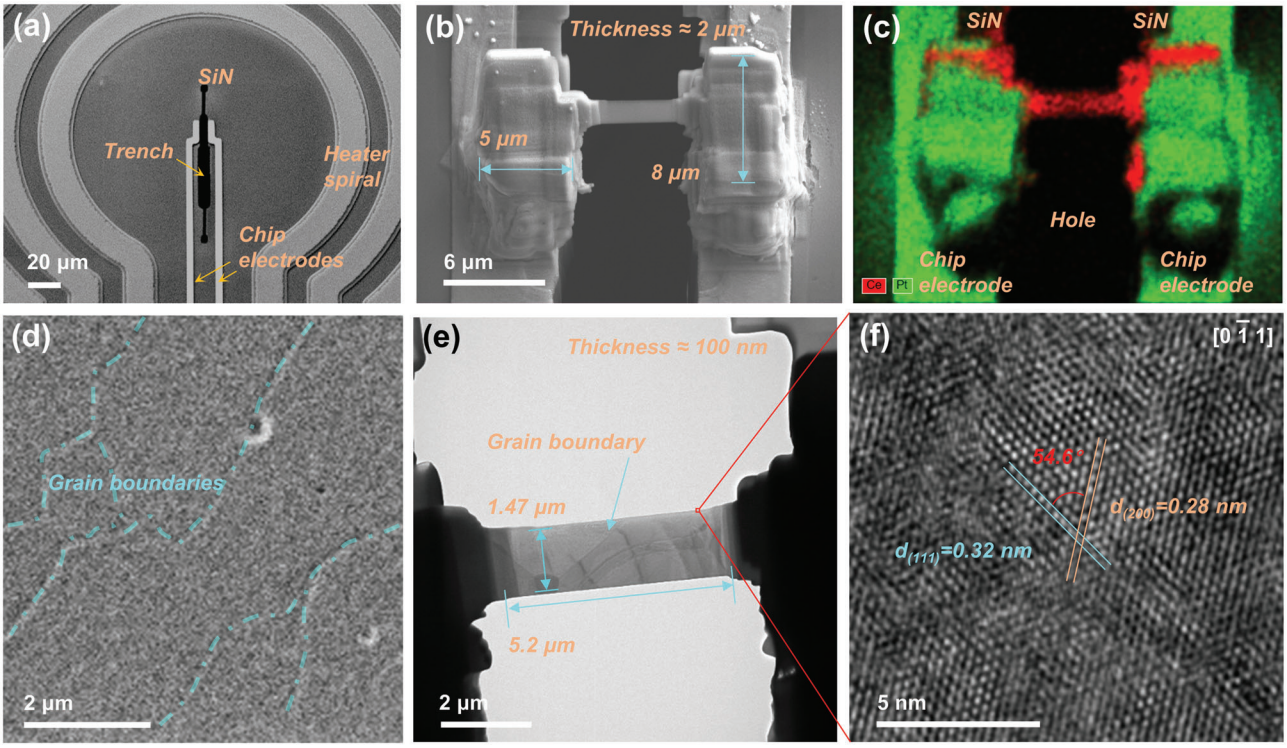

Figure 1. CGO sample mounted on a heating-biasing chip. a) SEM image showing the center of an empty heating-biasing chip; b) SEM image of the sample connected to the Pt electrodes of the chip; c) SEM-EDS map of (b) recorded at 15 kV, red color representing the Ce Lα-peak, green the Pt Mα peak; d) ion-beam image of the CGO pellet; e) TEM image of center part of (b); f) HRTEM image, including crystal analysis of the region in (e) indicated by a red square.

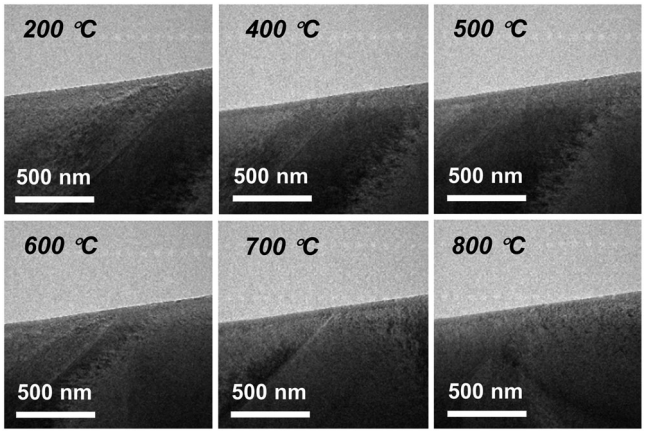

Figure 2. In situ TEM images of the CGO sample in H_2/H_2O with partial pressure ratio of 0.8 as a function of temperature.

2.3. EIS Electrical Circuit Model

Figure 3 presents Nyquist plots of the EIS data recorded in the three gas environments at temperatures from 500 °C to 800 °C. All spectra can be separated into two arcs. The electrical circuit model (ECM) presented in Figure 3 is used to fit the two arcs. These include resistances, R_t and R_p and constant phase elements, CPE_{shunt}, $CPE_{int,}$ and CPE_{chem}. The topology of the ECM and each of its elements is described in the following.

The CPE_{shunt} corresponds to the shunt capacitance from the electrical circuit on the MEMS chip, the TEM holder wires, and the cables connecting to the potentiostat. This is connected in parallel to the entire sample and all its contributions. The value of the CPE_{shunt} deduced from the measurements carried out with a sample matches indeed the capacitance recorded for an empty chip at each temperature from 500 °C to 800 °C, i.e., $\approx 3.8 \times 10^{-11}$ F.

The high-frequency arc starts at the origin of the real and imaginary axes at high frequencies and can be ascribed to ohmic transport through the central thin CGO part.

For a mixed conductor, such as CGO, the ohmic transport resistance, R_t is related to the movement of ions and electrons in the material, and therefore R_t has both an ionic and an electronic component as will be discussed in detail later. The transport resistance is denoted by R_t in the electrical circuit model (ECM). In principle, the ECM model should also include the bulk capacitance of the sample in parallel with R_t. For the present sample dimensions, the expected bulk capacitance is approximately 7.5×10^{-18} F m^{-1}, negligible in comparison to CPE_{shunt}, and therefore not included in the ECM.

The second arc can be associated with several possible contributions including transport barriers at grain boundaries,[15] gas diffusion and gas conversion contributions[16] or the surface exchange reaction. The grain boundary resistance[17] will be negligible for the present micrometer-sized sample with large grains, having only a few grain boundaries (only one visible in the central part (Figure 1e), and its expected capacitance ($\approx 10^{-13}$ F, see

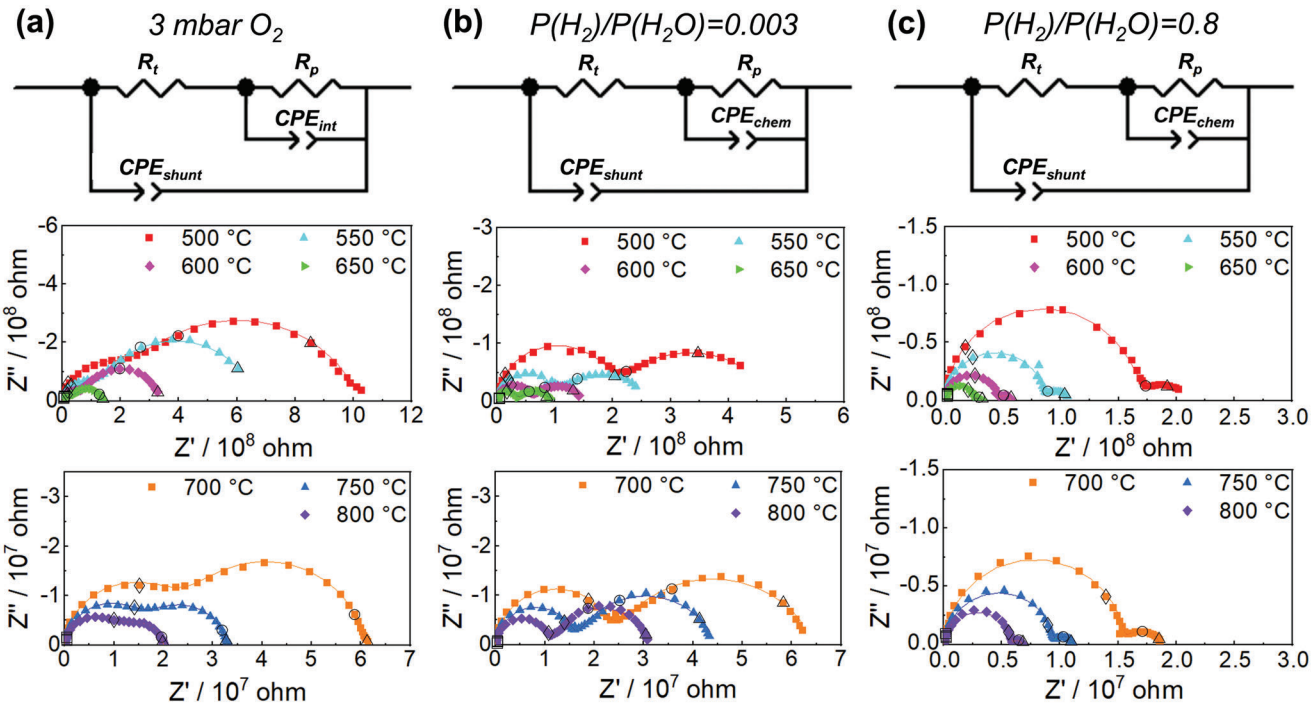

Figure 3. EIS spectra (symbols) and fittings (lines) recorded in a) O_2 (3 mbar) and in a H_2/H_2O with partial pressure ratio of b) 0.003 (total pressure 5 mbar) and c) 0.8 (total pressure 3 mbar); 10 kHz (square), 100 Hz (diamond), 1 Hz (circle), 0.1 Hz (triangle) are noted on the spectra, with hollow symbols; ECM used for fitting the data are presented at the top for each gas composition.

Section S6, Supporting Information)[18] is smaller than the measured shunt capacitance (≈10^{-11} F). Considering the small sample dimensions and the extremely small currents incited in it (≈10^{-10} A), gas concentration impedances are also negligible.[16] The low-frequency arc is therefore ascribed to the surface exchange reaction resistance, denoted by R_p. It is coupled to the gas–solid interface capacitance and the chemical capacitance of CGO, denoted by CPE_{int} and CPE_{chem}, respectively, in the ECM (Figure 3).

The ECM in Figure 3a is used to fit all spectra recorded in O_2, with CPE_{chem} of CGO being negligible, due to the very small concentration of small polarons (as discussed in Section S5, Supporting Information) and CPE_{int} being dominant. In H_2/H_2O, on the other hand, CPE_{chem} of CGO is expected to form a substantial contribution, which increases with increasing temperature and H_2-to-H_2O ratio to values substantially larger than CPE_{int}.[19]

From Figure 3, for all gas environments, it can be observed that the magnitude of both the first and second arc decreases as a function of temperature, indicating thermally activated processes as indeed expected for both the transport and surface reaction. This is also in line with a negligible gas concentration contribution that would be nearly temperature independent.

2.4. EIS Data Analysis

Both the conductivity and the surface exchange reaction of CGO depend on the gas environment. **Figure 4** presents a schematic illustration of the differences for our CGO TEM sample in O_2 and H_2/H_2O. The overall chemical reaction formulae are different in the two cases. Also, in O_2, CGO is a pure ionic conductor which limits the active surface close to the region of the electron-conducting Pt current collector. In the H_2/H_2O environment electrons are transported through the side parts of CGO thereby allowing the entire CGO surface to be active.

In this section we will therefore analyze the transport and surface exchange resistance from the EIS measurements in each type of gas environment separately, starting with the O_2 environment.

Using the following equation and the dimensions of the thinned central part of the sample, the total conductivity, σ_t, consisting of contributions from both ionic and electronic conductivity, can be calculated from R_t.

$$\sigma_t = \frac{1}{R_t}\frac{l}{w \cdot t} \quad (1)$$

where l, w and t are the length, width and thickness of the thin central part of the sample, respectively. Notice that only the thin central part is considered for calculating σ_t since it contributes to over 98% of the total transport resistance (see Section S7, Supporting Information). **Figure 5**a presents σ_t as a function of temperature in O_2, and is compared with reference data from bulk polycrystalline CGO in air.[20] From the slope of the fitted line in Figure 5a, an activation energy of $E_a = 0.7$ eV was determined, which is consistent with literature values: In 3 mbar O_2 and 500–800 °C, CGO is primarily an ionic conductor,[17b,21] and the determined E_a corresponds to that for the ionic conductivity, σ_{ion}. The present EIS-TEM deduced σ_t values in O_2 agree closely with the

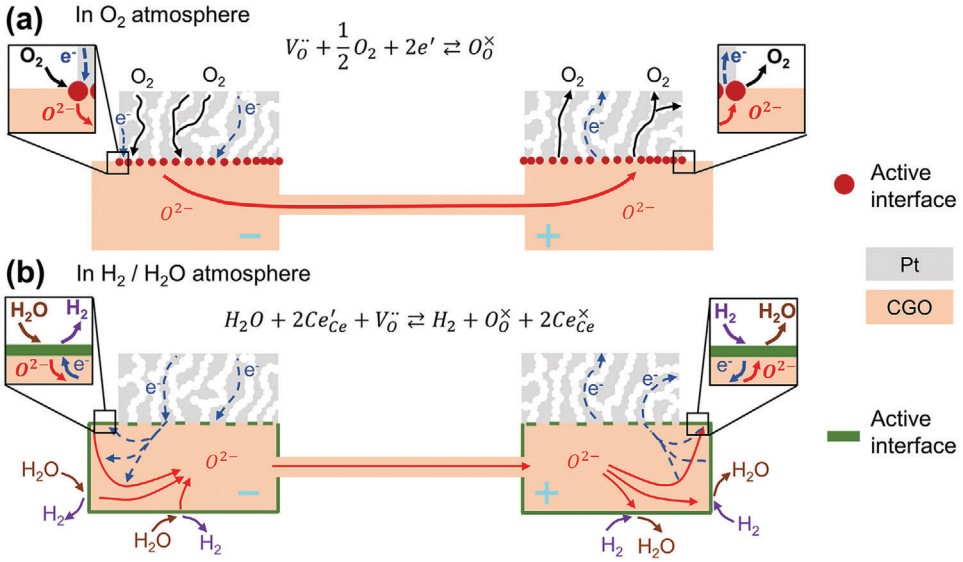

Figure 4. Illustration of active surface area for Pt-CGO as a) pure ionic conductor and as b) mixed electronic/ionic conductor. Arrows indicate the direction of ions (red) and electrons (Navy). In the actual experiment, the flow direction alternates with the frequency of the imposed AC perturbation.

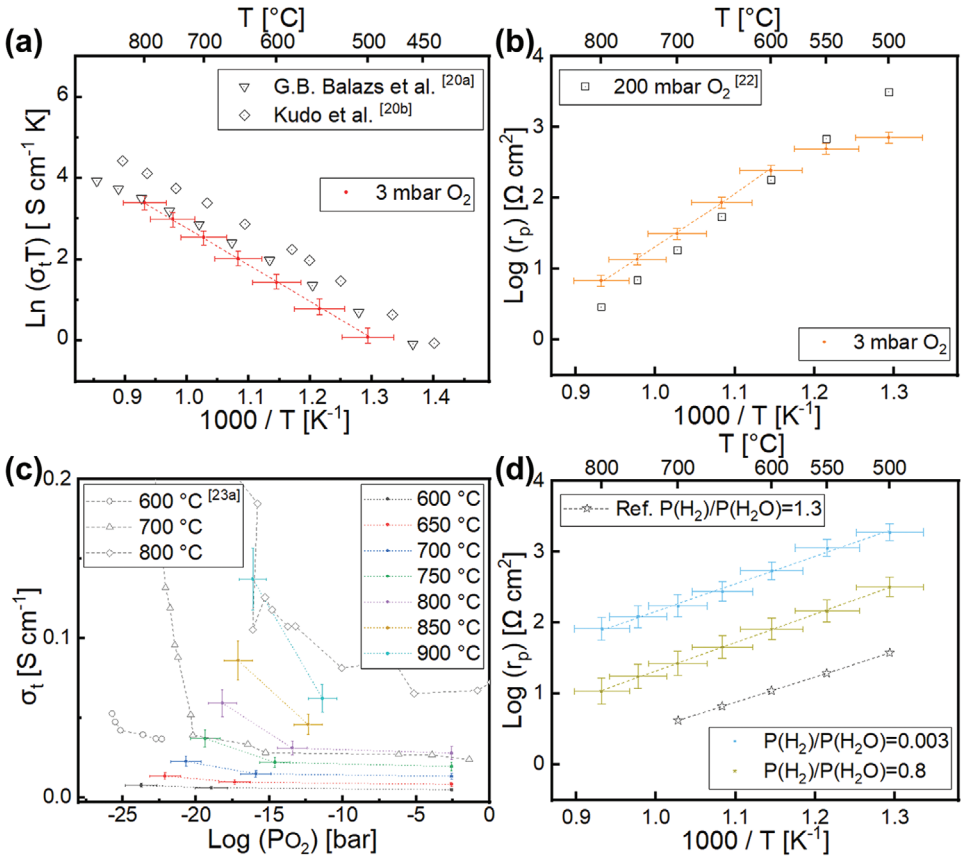

Figure 5. Electrochemical EIS-TEM measurements of CGO in different atmospheres. a) Arrhenius plot of total conductivity in 3 mbar O_2 (red) and reference data for bulk polycrystalline CGO in air (black);[20] b) Arrhenius plot of the surface reaction resistance in 3 mbar O_2 (orange), and reference data from a CGO thin film electrode in synthetic air (black);[22] c) total conductivity as a function of pO_2 (colored), and empty black symbols refer to reference data for polycrystalline CGO;[23a] d) surface reaction resistance as function of temperature in H_2/H_2O atmospheres (blue, green), and reference data from a CGO thin film electrode in H_2/H_2O with partial pressure ratio of 1.3 (black).[24]

reference data both with respect to E_a and to the absolute values for σ_t.

The resistance associated with the surface exchange reaction was also determined and compared to literature values. To quantify the area-specific surface reaction resistance, we need to estimate the active CGO surface. For a pure ionic conductor, like CGO in 3 mbar O_2, the oxygen exchange is expected to take place in a localized reaction zone near the triple phase boundary (TPB) consisting of the ion conductor (CGO), the electron conductor (Pt) and the gas phase. For the present sample, the TPB will therefore be close to the Pt current collector as illustrated in Figure 4a (red dots).[12,17a] As described in the experimental section, the Pt forms a nano-porous structure after the carbon removal pretreatment. Compared to a dense Pt, the nanoporous Pt will enhance the surface exchange reaction by an increased total TPB length. Perfect percolation through the nanoporous Pt cannot be expected and the surface exchange reaction will be prohibited where gas pores terminate before reaching the surface. This effect will be discussed later in this paper. The area-specific surface reaction resistance, r_p, can therefore be calculated by using Equation 2.

$$r_p = R_p * S \tag{2}$$

where S is the interface between CGO and the nanoporous Pt (around 92 μm^2). The result is presented as a function of temperature in Figure 5b in comparison with data from a dense CGO thin film model electrode tested in synthetic air. For the surface exchange reaction in O_2, E_a = 1.5 eV is deduced from the slope of Figure 5b for temperatures above 600 °C, a value that is close to the reference value of E_a = 1.7 eV for the CGO thin film electrode.[22] In the temperature range 500– 600 °C, the slope clearly deviates from the straight line, possibly because the total resistance of the nanoscaled CGO sample approached the Giga-ohm regime where a current leak through the chip starts to influence the measurements.

We will now focus on the experiments carried out in the H_2/H_2O environment. The electronic conductivity, σ_{elec} in CGO, depends strongly on the oxygen partial pressure as described by Equation 3.[23]

$$\sigma_t = \sigma_{ion} + \sigma_{elec} = \sigma_{ion} + \sigma^0_{elec} P_{O_2}^{-1/4} \tag{3}$$

where σ^0_{elec} can be regarded as a constant for small deviations from oxygen stoichiometry. At low oxygen partial pressures, CGO is therefore a mixed conductor with both oxygen vacancies and electrons as charge carriers.

Figure 5c presents σ_t as a function of oxygen partial pressure for the EIS-TEM measurements compared with reference data. The figure shows that σ_t increases with decreasing oxygen partial pressure, as expected according to Equation 3. Although the trend of σ_t is as expected, the absolute values deviate from the reference values. The σ_t measured at 700 °C and 750 °C matches well with the reference data at 600 °C and 700 °C, respectively.[23a] This could indicate an error in the measured temperature in the order of 50–100 °C which is higher than the 5% error on the temperature (corresponding to 35–38 °C for read-out temperatures 700–750 °C) expected for these commercials MEMS chips. A possible explanation is a temperature gradient across the thin central part of the sample due to the relatively low thermal conductivity of CGO.

To assess this hypothesis, a temperature calibration experiment was conducted based on the melting point of Zn nanoparticles deposited on a similar CGO lamella. When ramping the temperature up in 3 mbar H_2 at a rate of 20 °C min^{-1}, the in situ TEM images showed Zn melting at a ≈50 °C higher read-out temperature in the center compared to the sides of the sample (Figure S3 and Video S1, Supporting Information). This confirms that the temperature off-set observed in Figure 5c is most likely due to a temperature gradient across the CGO lamella. Additional work, which is beyond the scope of the present work, is needed to accurately calibrate or calculate the absolute temperature in different positions of the TEM sample as a function of nominal chip temperature.

The thicker side parts of the sample are not expected to deviate substantially from the nominal chip temperature (around 5% of read out value), and therefore the surface reaction rates and associated capacitances determined by EIS are expected to reflect a fairly accurate temperature dependence.

For the mixed conducting CGO in H_2/H_2O environments, the surface exchange reaction takes place not only near the TPB, but on the entire CGO–gas interface,[17a] as illustrated in Figure 4b (green line). The total surface area (S) of both thick side parts of the CGO (261 μm^2) is therefore used in Equation 2 to calculate the area-specific surface reaction resistance, r_p. The surface exchange resistance R_p determined from the second arc, however, is influenced by an electronic leak current through the thin central part of the MIEC CGO, i.e., not all the electrical current participates in the electrochemical reaction. This can be corrected using the following equation:[17a,24]

$$R_p^{cor} = \frac{R_p R_{elec}}{R_{elec} - R_p} - R_{ion} \tag{4}$$

where the ionic resistance, R_{ion}, represents the transport resistance recorded in O_2. The electronic resistance, R_{elec} is determined from, σ_{elec}, using the dimensions of the central part in Equation 1 and σ_{elec} is determined from σ_t and σ_{ion} via Equation 3. Finally r_p corrected for leak currents is calculated from R_p^{cor} using Equation 2. The effect of correcting for leak currents is shown in Figure S6 (Supporting Information).

Figure 5d shows the temperature dependence of the corrected r_p for CGO in H_2/H_2O with partial pressure ratio of 0.003 and 0.8. For both gas environments the measured E_a = 0.8 eV. This value is close to the reference value of 0.7 eV.[25] Also, the absolute values of r_p decrease with increasing H_2/H_2O ratio (Figure 5d), corresponding to a decreasing pO_2 and increasing electronic conductivity (Figure 5c). A number of studies suggest that the second electron transfer (likely coupled with the H-H association and desorption) is the rate-limiting step for the H_2 evolution reaction (HER) on ceria.[26] This will accelerate upon increasing the concentration of electronic charge carriers, resulting in reduced r_p upon increasing H_2/H_2O ratio as observed in the present experiment. A decrease in r_p upon increasing H_2/H_2O ratio is also expected for the H_2 oxidation reaction (HOR).[27]

The volume-specific capacitance, which can be calculated from CPE_{chem} by using Brug et al.'s formula and geometry of the CGO sample is presented in **Figure 6**.[28] Considering the 2000 nm

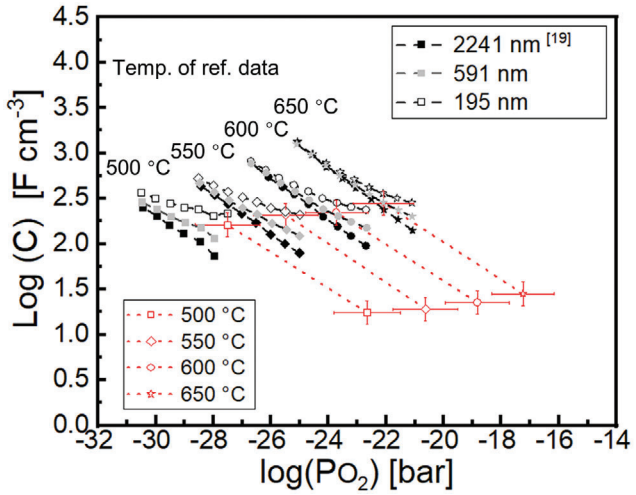

Figure 6. Volume-specific capacitance of the 2000 nm thick CGO side parts (red) as function of oxygen partial pressure and reference data from 2241 nm (black), 591 nm (gray), and 195 nm (black open symbols) CGO films at 500 °C, 550 °C, 600 °C, 650 °C, respectively.[19]

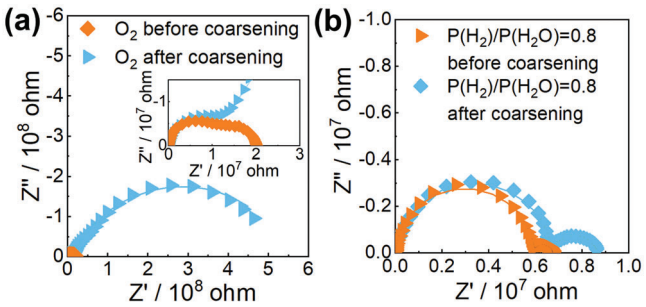

Figure 7. a) EIS spectra recorded in 3 mbar O_2 at 800 °C before and after coarsening; b) EIS spectra recorded in H_2/H_2O with partial pressure ratio of 0.8 at 800 °C before and after coarsening.

thick side parts, our results for 600 °C and 650 °C match well with the reference data of the film with a similar thickness of 2241 nm.[19] Both of them follow the $P_{O_2}^{-1/4}$ dependence as expected, and this confirms that the capacitance is dominated by the chemical capacitance.

2.5. The Effect of Porous Pt

In order to explore the effect of the nanoporous Pt structure in the electrochemical measurements, the CGO sample was exposed to 900 °C in the reducing gas environment (An overview of all EIS-TEM processes for the sample is shown in Section S9, Supporting Information). These conditions lead to Pt coarsening (Figure S2c, Supporting Information), loss of percolating pore network for gas diffusion and thereby decreased TPB length. It can therefore be expected that the surface exchange resistance is increased, in particular for the reaction in oxygen where the surface reaction rate depends directly on the TPB. This effect was confirmed by a comparison of EIS spectra recorded before and after coarsening (**Figure 7**a). The transport resistivity is rather similar (i.e., 35 Ω cm before and 39 Ω cm after) while the surface reaction resistance increased 74 times (to 492 Ω cm^2 from 7 Ω cm^2).

The effect of coarsening on the surface exchange reaction it is expected to be smaller in H_2/H_2O because here the entire CGO surface is active (as illustrated in Figure 4b). This is confirmed by the EIS spectra in Figure 7b. In H_2/H_2O with ratio of 0.8, the transport resistivity after coarsening (19 Ω cm) is similar to the value measured before (17 Ω cm). The surface reaction resistance after coarsening (5 Ω cm^2) is only 2.5 times larger than before (2 Ω cm^2).

2.6. Reproducibility of Test Results

The analysis above shows that the Pt morphology determines the TPB and influences the surface exchange reaction resistance in O_2. For comparison, two additional CGO samples with a smaller Pt-CGO interface, and therefore shorter TPB, were produced and tested (**Figure 8**). In H_2/H_2O with gas pressure ratio 0.003, the area-specific surface reaction resistance of the CGO sample 1 and 2 were compared and the absolute values agree well, deviating only by a factor of ≈2 (Figure 8b). The transport resistivity deviates more, by a factor of ≈5 (Figure 8c). This can be attributed to the different temperature distributions across the center part of the samples, as a consequence of the different sample geometries (Figures 1 and 8a). The transport resistance is dominated by the thin central part which also happens to be the part influenced the most by the temperature gradient. CGO sample 3 is tested in both 3 mbar O_2 and H_2/H_2O with a partial pressure ratio of 0.8. The activation energy and absolute values of the area-specific surface reaction resistance match well with CGO sample 1 in both atmospheres (Figure 8d,e). The transport resistivity in H_2/H_2O with a partial pressure ratio of 0.8 shows a relatively small deviation in the absolute value by a factor of 3 (Figure 8f). Again, this can be explained by the different temperature distributions across the two samples.

Overall, we observe good reproducibility with respect to both transport properties and surface exchange reaction resistances in O_2 and H_2/H_2O amongst the three samples (Figure 8), and any deviations can be rationalized by the somewhat different temperature distributions across the different samples. These results showcase the possibility to carry out operando EIS-TEM studies on SOC samples and open up the path for the investigation of full cells to answer questions of great technological significance.

3. Conclusion

The feasibility of operando EIS-TEM on solid-state electrochemical cells operating in reactive gasses and elevated temperatures was demonstrated by measuring the temperature and pO_2 dependence of the ionic and electronic conductivity of CGO, as well as its surface exchange resistivity in O_2 and H_2/H_2O atmospheres, and its volume-specific chemical capacitance in H_2/H_2O.

A special sample structure was designed with thick side parts and a thin central part, by which one can separate the contributions of bulk charge transport and the surface reaction processes. The measured temperature and pO_2-dependent conductivity, surface exchange resistance, and chemical capacitance, as well as their activation energies and pO_2 exponents are found to agree well with reference data.

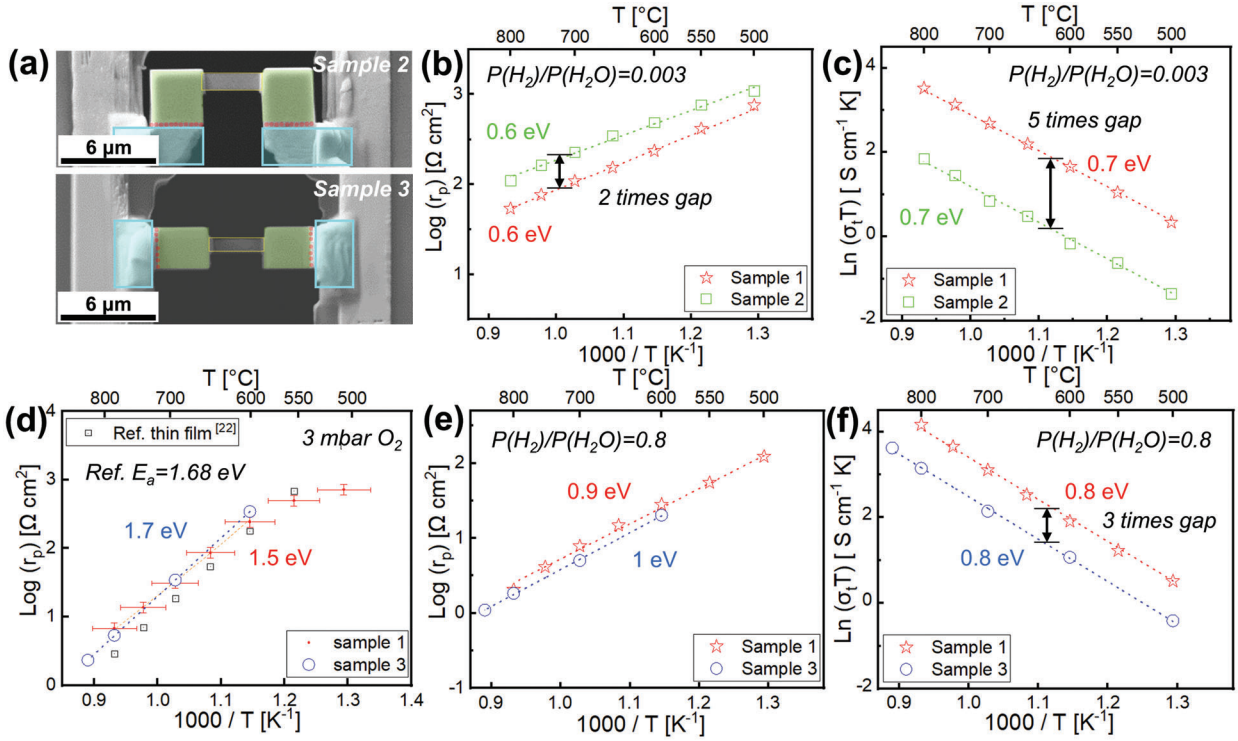

Figure 8. Comparison of electrochemical EIS-TEM measurements of CGO samples 2 and 3 in different atmospheres relative to CGO sample 1. a) SEM images of samples 2 and 3; the thin central part, thick side parts, and deposited Pt are marked by yellow, green and cyan colors respectively. In H_2/H_2O atmospheres, the surface exchange reaction takes place at the surface of the side parts (green), while in oxygen atmosphere, the surface exchange reaction only take place at the Pt-CGO interface (red); b) comparing the area specific surface reaction resistance of sample 1 and 2 in H_2/H_2O with gas partial pressure ratio of 0.003; c) the total conductivity in H_2/H_2O with partial pressure ratio of 0.003 for sample 1 and 2; d) the area specific surface reaction resistance of sample 1 and 3 in 3 mbar O_2, and reference data from a CGO thin film electrode in synthetic air (black);[22] e) area-specific surface reaction resistance in H_2/H_2O with partial pressure ratio of 0.8 for samples 1 and 3; f) the total conductivity in H_2/H_2O with partial pressure ratio of 0.8 for sample 1 and 3.

It can therefore be concluded that reliable EIS measurements can be performed in the TEM, even for the difficult case of hard, brittle ceramic materials which are thinned sufficiently for HRTEM analysis. The strength of operando EIS-TEM is that it allows us to simultaneously gain information on both the electrochemical behavior and the structure/composition of a material at the atomic level, in its active state.

With the purpose of determining the validity of the EIS measurements in the TEM, we have deliberately chosen operation conditions (temperatures, gas environments, polarizations) where the material was stable. The EIS-TEM method will be of particular importance in the investigation of dynamical changes of the structure and composition induced by the operating conditions. For such cases, the effect of the dynamical changes observed from the TEM can be directly compared to simultaneously recorded EIS spectra. Such a capability will be crucial for the further development in our understanding of the nanoscale processes such as degradation in a number of green energy technologies, e.g., electrolysis cells, fuel cells, and batteries.

4. Experimental Section

Sintered Pellet Preparation: Commercial ultrahigh surface (UHS) area $Ce_{0.9}Gd_{0.1}O_{1.95-\delta}$ (CGO) powder was purchased from Solvay. The powder was compressed into pellets using a 10 mm diameter stainless steel mold at a uniaxial pressure of 3 MPa, followed by isostatic pressing at 325 MPa and sintering at 1500 °C in air for 12 h and slow cooling to room temperature at a rate of 0.5 K min^{-1}. The geometrical density of the pellets was between 94 and 97% of the theoretical density.[12]

TEM Sample Preparation: By using a focused Ga^+ ion beam (Crossbeam, ZEISS, 1540XB) and a micromanipulator (Kleindiek), TEM lamellas were prepared from the CGO pellet and were mounted on heating-biasing chips (DENS lightning, with 4 contacts for heating, 2 contacts for biasing, and a through-hole window). To avoid any current leak along the surface of the chip due to Pt overspray, the two Pt electrodes of the chip were further separated by milling a long trench between them before mounting the TEM lamella (Figure 1 and Figure S1, Supporting Information). After the mounting process, the CGO lamellas have a 10° angle relative to the chip surface. Pt was ion-deposited to ensure electrical contact between the CGO lamella and the Pt electrodes at the chip. A final preparation step was thinning and polishing the central part of the lamella to allow for TEM analysis and to remove any Pt overspray from ion deposition.[29] A result of such sample preparation is presented in Figure 1.

EIS-TEM Experiments: The EIS-TEM experiments were carried out in an ETEM (Titan 80-300 kV) equipped with a differential pumping system and an image aberration corrector (FEI Europe, Netherlands).[30] The ETEM can host gases like O_2, H_2 and H_2O with partial pressures from 10^{-6} to 26 mbar. With the use of needle valves and mass flow controllers, the mixing of two or more of these gases can be achieved and the partial pressures can be controlled. For our experiments, low oxygen partial pressures were achieved by mixing H_2 and H_2O vapor. The experiments were carried out in three different gas environments: a) 3 mbar O_2, b) a H_2/H_2O mixture with partial pressure ratio of 0.003 (total pressure 5 mbar), and c) a H_2/H_2O with partial pressure ratio of 0.8 (total pressure 3 mbar).

The electrochemical workstation (Gamry FAS2 Femtostat) used for two-probe EIS measurements was connected to the Pt electrodes of the chip via the TEM holder (DENS Lightning). EIS was performed by applying an alternating voltage amplitude of 20 mV in a frequency range from 100 kHz to 0.03 Hz.

Before EIS-TEM measurements, the samples were heated to 500 °C in the ETEM at 3 mbar O_2 for 5 min. This is to remove the amorphous carbon and its potential effects, which is mixed with the Pt nanoparticles in the ion-deposited Pt.[29,31] EELS analysis showed that the carbon edge was fully removed after this treatment, confirming that the treatment was sufficient to remove the carbon. After this, the Pt forms a nano-porous network with voids in the regions that previously contained carbon (Figure S2a,b, Supporting Information).

EIS-TEM analysis was carried out while the temperature was held constant at 500–900 °C, in steps of 50 °C, after waiting for 3 min for the system to stabilize at each temperature. The total time spent on image acquisition and impedance measurement at each temperature was ≈12 min.

For all operando TEM experiments, it is important to minimize possible effects of the electron beam. Therefore, a relatively low beam current density of 23 e $Å^{-2}$ s^{-1} or lower was used for TEM imaging, except for HRTEM which was recorded only once at RT. The beam was also blanked during temperature ramping and EIS analysis. No changes in the sample morphology or in the Ce oxidation state were observed as a result of beam exposure according to imaging and EELS analysis.

Error Analysis: Errors on reported calculated data can come from the measurement of sample dimensions, gas pressure and temperature, and EIS recording and fitting. All these errors are considered and presented as error bars in the graphs. The details of the error analysis are presented in the Supporting Information.

Supporting Information

Supporting Information is available from the Wiley Online Library or from the author.

Acknowledgements

Z.M. and W.L.D. contributed equally to this work. S.B.S. planned and initiated the project. Z.M. and W.L.D. contributed to development of the EIS-TEM experimental procedures. Z.M. prepared the TEM samples and conducted the operando EIS-TEM experiments and corresponding data analysis. Z.M., W.L.D., F.M.C., W.Z., S.B.S, C.C., and K.S.M. all contributed to the discussions for the development of experimental method and of interpretation of the results. Z.M. and W.L.D. prepared the figures. Z.M., W.L.D., S.B.S., C.C., K.S.M., F.M.C., and W.Z. wrote the manuscript and all the authors contributed to the discussion and revision of the manuscript. This project was received funding from the European Research Council under the European Union's Horizon 2020 research and innovation programme (grant agreement No 850850).

Conflict of Interest

The authors declare no conflict of interest.

Data Availability Statement

The data that support the findings of this study are openly available at https://doi.org/10.11583/DTU.22347127.v1.

Keywords

CGO, EIS, ETEM, operando, SOEC, SOFC

Received: December 29, 2022
Revised: February 27, 2023
Published online: April 10, 2023

[1] A. Hauch, R. Küngas, P. Blennow, A. B. Hansen, J. B. Hansen, B. V. Mathiesen, M. B. Mogensen, *Science* **2020**, *370*, eaba6118.

[2] a) L. Holzer, B. Iwanschitz, T. Hocker, B. Münch, M. Prestat, D. Wiedenmann, U. Vogt, P. Holtappels, J. Sfeir, A. Mai, T. Graule, *J. Power Sources* **2011**, *196*, 1279; b) S.-K. Jung, H. Gwon, J. Hong, K.-Y. Park, D.-H. Seo, H. Kim, J. Hyun, W. Yang, K. Kang, *Adv. Energy Mater.* **2014**, *4*, 1300787; c) B.-K. Park, Q. Zhang, P. W. Voorhees, S. A. Barnett, *Energy Environ. Sci.* **2019**, *12*, 3053.

[3] a) R. T. K. Baker, C. Thomas, R. B. Thomas, *J. Catal.* **1975**, *38*, 510; b) R. T. K. Baker, R. B. Thomas, M. Wells, *Carbon* **1975**, *13*, 141; c) P. A. Crozier, A. K. Datye, in *Studies in Surface Science and Catalysis*, Vol. *130* (Eds: A. Corma, F. V. Melo, S. Mendioroz, J. L. G. Fierro), Elsevier, Granada, Spain **2000**, p. 3119; d) P. L. Hansen, J. B. Wagner, S. Helveg, J. R. Rostrup-Nielsen, B. S. Clausen, H. Topsoe, *Science* **2002**, *295*, 2053; e) S. Helveg, C. López-Cartes, J. Sehested, P. L. Hansen, B. S. Clausen, J. R. Rostrup-Nielsen, F. Abild-Pedersen, J. K. Nørskov, *Nature* **2004**, *427*, 426; f) S. B. Simonsen, I. Chorkendorff, S. Dahl, M. Skoglundh, J. Sehested, S. Helveg, *J. Am. Chem. Soc.* **2010**, *132*, 7968; g) P. A. Crozier, S. Chenna, *Ultramicroscopy* **2011**, *111*, 177; h) S. Chenna, P. A. Crozier, *ACS Catal.* **2012**, *2*, 2395; i) J. R. Jinschek, *Chem. Commun.* **2014**, *50*, 2696; j) S. B. Simonsen, Y. Wang, J. O. Jensen, W. Zhang, *Nanotechnology* **2017**, *28*, 475710.

[4] a) R. Sinclair, M. A. Parker, *Nature* **1986**, *322*, 531; b) K. Holloway, R. Sinclair, *J. Less-Common Met.* **1988**, *140*, 139; c) T. Kamino, H. Saka, *Microsc., Microanal., Microstruct.* **1993**, *4*, 127.

[5] a) M. Legros, *C. R. Phys.* **2014**, *15*, 224; b) Y. Deng, R. Zhang, T. C. Pekin, C. Gammer, J. Ciston, P. Ercius, C. Ophus, K. Bustillo, C. Song, S. Zhao, H. Guo, Y. Zhao, H. Dong, Z. Chen, A. M. Minor, *Adv. Mater.* **2020**, *32*, 1906105.

[6] a) R. J. Kamaladasa, A. A. Sharma, Y.-T. Lai, W. Chen, P. A. Salvador, J. A. Bain, M. Skowronski, Y. N. Picard, *Microsc. Microanal.* **2015**, *21*, 140; b) B. Haas, J.-L. Rouvière, V. Boureau, R. Berthier, D. Cooper, *Ultramicroscopy* **2019**, *198*, 58.

[7] M. J. Jørgensen, M. Mogensen, *J. Electrochem. Soc.* **2001**, *148*, A433.

[8] a) S. Basak, K. Dzieciol, Y. E. Durmus, H. Tempel, H. Kungl, C. George, J. Mayer, R.-A. Eichel, *Chem. Phys. Rev.* **2022**, *3*, 031303; b) M. J. Williamson, R. M. Tromp, P. M. Vereecken, R. Hull, F. M. Ross, *Nat. Mater.* **2003**, *2*, 532; c) X. H. Liu, J. Y. Huang, *Energy Environ. Sci.* **2011**, *4*, 3844.

[9] a) A. H. Tavabi, S. Arai, S. Muto, T. Tanji, R. E. Dunin-Borkowski, *Microsc. Microanal.* **2014**, *20*, 1817; b) F. Gualandris, S. B. Simonsen, J. B. Wagner, S. Sanna, S. Muto, L. T. Kuhn, *ECS Trans.* **2017**, *75*, 123.

[10] a) S. H. Jo, P. Muralidharan, D. K. Kim, *Solid State Ionics* **2008**, *178*, 1990; b) T. Klemensø, J. Nielsen, P. Blennow, Å. H. Persson, T. Stegk, B. H. Christensen, S. Sønderby, *J. Power Sources* **2011**, *196*, 9459; c) J. Nielsen, T. Klemensø, P. Blennow, *J. Power Sources* **2012**, *219*, 305; d) E. M. Sala, N. Mazzanti, M. B. Mogensen, C. Chatzichristodoulou, *Solid State Ionics* **2022**, *375*, 115833.

[11] T. Malis, S. C. Cheng, R. F. Egerton, *J. Electron. Microsc. Tech.* **1988**, *8*, 193.

[12] C. Chatzichristodoulou, S. Ricote, S. P. V. Foghmoes, J. Glasscock, A. Kaiser, P. V. Hendriksen, *Solid State Ionics* **2015**, *269*, 51.

[13] a) V. Esposito, D. W. Ni, Z. He, W. Zhang, A. S. Prasad, J. A. Glasscock, C. Chatzichristodoulou, S. Ramousse, A. Kaiser, *Acta Mater.* **2013**, *61*, 6290; b) J. Chen, M. Ouyang, P. Boldrin, A. Atkinson, N. P. Brandon, *ACS Appl. Mater. Interfaces* **2020**, *12*, 47564.

[14] a) B. Goris, S. Turner, S. Bals, G. Van Tendeloo, *ACS Nano* **2014**, *8*, 10878; b) S.-G. Frederik, *Master thesis*, DTU Energy, DTU, Kgs. Lyngby, **2020**; c) R. Sinclair, S. C. Lee, Y. Shi, W. C. Chueh, *Ultramicroscopy* **2017**, *176*, 200.
[15] a) X. Guo, R. Waser, *Prog. Mater. Sci.* **2006**, *51*, 151; b) Y. Lin, S. Fang, D. Su, K. S. Brinkman, F. Chen, *Nat. Commun.* **2015**, *6*, 6824.
[16] P. Marmet, L. Holzer, J. G. Grolig, H. Bausinger, A. Mai, J. M. Brader, T. Hocker, *Phys. Chem. Chem. Phys.* **2021**, *23*, 23042.
[17] a) W. Lai, S. M. Haile, *J. Am. Ceram. Soc.* **2005**, *88*, 2979; b) X. Guo, W. Sigle, J. Maier, *J. Am. Ceram. Soc.* **2003**, *86*, 77.
[18] D. Pérez-Coll, E. Céspedes, A. J. Dos santos-García, G. C. Mather, C. Prieto, *J. Mater. Chem. A* **2014**, *2*, 7410.
[19] W. C. Chueh, S. M. Haile, *Phys. Chem. Chem. Phys.* **2009**, *11*, 8144.
[20] a) G. B. Balazs, R. S. Glass, *Solid State Ionics* **1995**, *76*, 155; b) T. Kudo, H. Obayashi, *J. Electrochem. Soc.* **1975**, *122*, 142.
[21] C. Chatzichristodoulou, P. V. Hendriksen, *Phys. Chem. Chem. Phys.* **2011**, *13*, 21558.
[22] N. Mazzanti, *in submission* **2022**.
[23] a) S. Wang, T. Kobayashi, M. Dokiya, T. Hashimoto, *J. Electrochem. Soc.* **2000**, *147*, 3606; b) M. Mogensen, N. M. Sammes, G. A. Tompsett, *Solid State Ionics* **2000**, *129*, 63.
[24] J. Jamnik, J. Maier, *J. Electrochem. Soc.* **1999**, *146*, 4183.
[25] N. Mazzanti, *Ph.D. thesis* , DTU Energy, DTU, Kgs. Lyngby, **2021**.
[26] a) Z. A. Feng, F. El Gabaly, X. Ye, Z.-X. Shen, W. C. Chueh, *Nat. Commun.* **2014**, *5*, 4374; b) T. Wu, Q. Deng, H. A. Hansen, T. Vegge, *J. Phys. Chem. C* **2019**, *123*, 5507.
[27] Y. Choi, S. K. Cha, H. Ha, S. Lee, H. K. Seo, J. Y. Lee, H. Y. Kim, S. O. Kim, W. Jung, *Nat. Nanotechnol.* **2019**, *14*, 245.
[28] G. J. Brug, A. L. G. van den Eeden, M. Sluyters-Rehbach, J. H. Sluyters, *J. Electroanal. Chem. Interfacial Electrochem.* **1984**, *176*, 275.
[29] Y.-W. Lan, W.-H. Chang, Y.-C. Chang, C.-S. Chang, C.-D. Chen, *Nanotechnology* **2015**, *26*, 055705.
[30] T. W. Hansen, J. B. Wagner, J. R. Jinschek, R. E. Dunin-Borkowski, *Microsc. Microanal.* **2009**, *15*, 714.
[31] L.-j. Liu, J.-j. Wang, presented at *2001 6th Int. Conf. on Solid-State Integrated Circuit Technol. Proc. (Cat. No.01EX443)*, Shanghai, China, October **2001**.

